# Origin and Tuning of Bandgap in Chiral Phononic Crystals

Wei Ding, Rui Zhang, Tianning Chen, Shuai Qu, Dewen Yu, Liwei Dong, Jian Zhu, Yaowen Yang, Badreddine Assouar

# Origin and Tuning of Bandgap in Chiral Phononic Crystals

*Wei Ding[1, 2, †], Rui Zhang[1, †], Tianning Chen[1], Shuai Qu[2,3], Dewen Yu[1, 2], Liwei Dong[2,4], Jian Zhu[1, *], Yaowen Yang[2, *], Badreddine Assouar[5, *]*

[1]School of Mechanical Engineering and State Key Laboratory of Strength & Vibration of Mechanical Structures, Xi'an Jiaotong University, Xi'an, Shaanxi 710049, P.R. China

[2]School of Civil and Environmental Engineering, Nanyang Technological University, 50 Nanyang Avenue, 639798 Singapore, Singapore

[3]Train and Track Research Institute, State Key Laboratory of Rail Transit Vehicle System, Southwest Jiaotong University, Chengdu, 610031, China

[4]Institute of Rail Transit, Tongji University, Shanghai, 201804, China

[5]Université de Lorraine, CNRS, Institut Jean Lamour, F-54000 Nancy, France

*Corresponding authors: jianzhuxj@xjtu.edu.cn (J. Zhu), cywyang@ntu.edu.sg (Y. Yang), badreddine.assouar@univ-lorraine.fr (B. Assouar).

† These authors contributed equally

**Abstract**

The wave equation revealing the wave propagation in chiral phononic crystals, established through force equilibrium law, conceals the underlying physical information, such as the essence of the motion coupling and the inertial amplification effect. This has led to a controversy over the bandgap mechanism. In this article, we theoretically unveil the reason for this controversy, and put forward an alternative approach from wave behavior to formulate the wave equation, offering an alternative pathway to articulate the bandgap physics directly. Based on the physics revealed by our theory method, we identify the obstacles in coupled acoustic and optic branches to widen and lower the bandgap. Then we introduce an approach based on spherical hinges to decrease the barriers, for customizing the bandgap frequency and width. Finally, we validate our proposal through numerical simulation and experimental demonstration.

**Keywords:** bandgap origin, bandgap customization, elastic waves, chiral phononic crystal

## Introduction

The bandgap property in phononic crystals (PnCs) is associated with extreme spatial dispersion [1], wave guidance [2, 3], and thermal physics [4]. Therein, since the inertial amplification effect induced by chirality, which is beneficial for lowering the bandgap beyond the barriers constrained by mass and stiffness [5, 6, 7], enables the chiral PnCs the superior performance at low-frequency regime, thus expanding its applicable scope in the elastic-wave fields [8, 9]. The inertial amplification concept in the mechanical perspective presented in the seminal study of Yilmaz refers to a dynamic virtual inertia attached to a static mass, thus reducing the eigenfrequency of the system [10]. However, the bandgap mechanism of chiral PnCs has always been controversial [11, 12, 13]. The seminal theories have indicated the inertial amplification as the mechanism behind such a bandgap [14, 15], while different chirality assemblies have different dispersion spectrum [14, 16]. Therefore, the mechanism has been attributed to inertial amplification and the relative orientation of adjacent chiral centers in the syndiotactic system [14].

More recently, two explanations have been reported for a physical explanation. The first is the dimer chain [13], where coupling longitudinal and torsional waves is similar to the coupled transverse and rotational waves in the periodic mass-spring system [17]. The study [13] concluded that a monatomic chain effect, i.e., the so-called inertial amplification method, cannot support the bandgap phenomenon. The second explanation is related to analogous Thomson scattering [12] to consolidate the inertial amplification claim [15]. In addition, the analogous Thomson scattering[12] physically detailed that inertial amplification of this chiral sub unit cell is induced by coupling two or more polarizations in the same lumped mass and chirality is to achieve the secondary scattering for destructive interferences. These two theoretical interpretations are plausible because of the validation, yet they are contradictory since the debate about the existence or absence of inertial amplification.

Here, we develop a theoretical analysis based on the wave behavior in chiral PnCs, to clarify the cause of the contradictory and unify and refine the bandgap mechanisms. We demonstrate that the wave equation directly derived from force equilibrium law will conceal the underlying physics, e.g., inertial amplification. Our method allows to articulate bandgap physics, and calculate the transmission simultaneously. In contrast to the conventional theoretical method [6, 10, 18], it allows observing the fundamental physical parameters of acoustic and optic modes under the assumption of elastic ligaments, i.e., inertial amplification coefficient, bending stiffness, stretch stiffness, and their origins and interactions. Our analysis pointed out that the rise of the inertial amplification coefficient is closely related to the bending and stretch stiffness. Consequently, the bandgap width and the reduction of the starting frequency are

mutually constrained, which poses a significant challenge to the realization of wide subwavelength bandgaps (the effects of the geometrical dimensions, characterized in equivalent stiffness [19] and equivalent mass [20, 21], are considered in normalization). To transcend this barrier, the spherical hinges and the spiral springs are employed to partial-decouple these coupled physical parameters. The numerical and experimental results validate the correctness and the feasibility of our proposals in the theory and geometrical mode.

## Results

### a) Theoretical Observation of Bandgap Origin

In the chiral subunit cell (Figure 1(a)), if there is a longitudinal input $\boldsymbol{P_I}$ on disk1 ($\boldsymbol{P_I} = \boldsymbol{A_1 e^{-i(wt+\phi_1)}}$, where $\boldsymbol{\phi_1} = \boldsymbol{0}$), the motion provided by $\boldsymbol{P_I}$ will propagate in the bending deformation (Figure 1(c)) and stretch deformation (Figure 1(d)) of the ligaments simultaneously. Neglecting the local deformation of the ligaments and disks, we can observe two polarizations at disk Ⅱ, i.e., longitudinal polarization $\boldsymbol{P_l}$ ($\boldsymbol{P_{lb} + P_{ls}}$) and rotational polarization $\boldsymbol{P_r}$ ($\boldsymbol{P_{rb} + P_{rs}}$) (where $\boldsymbol{P_{ij}}$ denotes that the $\boldsymbol{j^{th}}$ deformation mode of the ligaments induces the $\boldsymbol{i^{th}}$ polarization of the disk. In detail, subscript $\boldsymbol{i}$ can be longitudinal polarization $\boldsymbol{l}$ or rotational polarization $\boldsymbol{r}$. Subscript $\boldsymbol{j}$ denotes the $\boldsymbol{j^{th}}$ deformation mode of the ligaments, which can be bending mode $\boldsymbol{b}$ or stretch mode $\boldsymbol{s}$).

In the scenario of Figure 1(c), based on the right-hand spiral rule, the disk II will have a longitudinal polarization along $+z$-axis ($P_{lb}$) and a rotation polarization around $+z$-axis ($P_{rb}$) due to the bending mode. While in the scenario denoted by Figure 1(d), the disk 2 will have $-z$-axis rotational polarization ($P_{rs}$) in addition to the $+z$-axis longitudinal polarization ($P_{ls}$) due to the stretch mode. In short, there must be 4 polarizations in disk II, i.e., $P_{lb}$, $P_{rb}$, $P_{ls}$, and $P_{rs}$. Therein, the longitudinal polarization $P_{lb}$ and $P_{ls}$ vibrate in the same frequency and initial directions, while the rotational polarization $P_{rb}$ and $P_{rs}$ have the same frequency but opposite initial directions.

Because $P_{lb}$ and $P_{rb}$ are resulted from the bending deformation of the ligaments, they will have the same frequency and the same phase at any time. Therefore, for the $i^{th}$ lumped mass, assuming an extremely small harmonic displacement (Otherwise, there will be nonlinearity in this chiral unit cell [5]), $P_{lb}$ and $P_{rb}$ are linearly correlated by the inertial amplification coefficient $p$, as illustrated by Eq. (1).

$$U_i^l = u_i^l + \psi_i^l = {A_i}^l e^{-i(wt+\varphi_i^l)} + p\left(A_{i-1}^l e^{-i(wt+\varphi_{i-1}^l)} - {A_i}^l e^{-i(wt+\varphi_i^l)}\right), \quad (1)$$

where $p$ denotes the conversion coefficient from longitudinal polarization $P_{lb}$ to rotational polarization $P_{rb}$ and it is characterized as the inertial amplification coefficient in the inertia matrix [12, 15]. $u_i^l$ refers to longitudinal polarization induced longitudinal displacement and $\psi_i^l$ refers to longitudinal polarization induced rotational

displacement. $A_i^l$ implies the translational amplitude of the $i$th lumped mass. The superscript $l$ indicates that the longitudinal polarization $u$ and rotational polarization $\psi$ originate from the longitudinal mode. $\varphi$ refers to the initial phase.

Like $P_{lb}$ and $P_{rb}$, for the $i^{th}$ lumped mass, $P_{rs}$ and $P_{ls}$ satisfy

$$U_i^s = u_i^s + \psi_i^s = {\theta_i}^s e^{-i(wt+\varphi_i^s)} + q\left(\theta_{i-1}^s e^{-i(wt+\varphi_{i-1}^s)} - {\theta_i}^s e^{-i(wt+\varphi_i^s)}\right), \quad (2)$$

where $q$ indicates the conversion coefficient from longitudinal polarization $P_{ls}$ to rotational polarization $P_{rs}$. Because the sense of $q$ is exactly opposite to that of $p$, $q = \frac{1}{p}$ (see **Supplementary Note4** for more details). The superscript $s$ indicates that the longitudinal polarization $u$ and rotational polarization $\psi$ originate from the stretch mode.

Because the stretch stiffness $k_s$ is different from the bending stiffness $k_b$, $P_{rb}$ and $P_{rs}$ must have different phases, i.e., $\varphi^l \neq \varphi^s$, as do $P_{lb}$ and $P_{ls}$. This means $P_{lb} + P_{rb}$ and $P_{ls} + P_{rs}$ must be two independent wave modes, although we can only see the macroscopic results of longitudinal movement $P_l$ ($P_{lb} + P_{ls}$) and $P_r$ ($P_{rb} + P_{rs}$)) rotational movement rather than the results of $P_{lb} + P_{rb}$ and $P_{ls} + P_{rs}$.

Therefore, generally, in the global coordinate system, for the $i^{th}$ lumped mass, the longitudinal displacement $u$ is determined as

$$u_i = u_i^l + u_i^s = A_i^l e^{-i(wt+\varphi_i^l)} + (-1)^i A_i^s e^{-i(wt+\varphi_i^s)}, \quad (3)$$

and the rotational displacement $\vartheta$ is determined as

$$\vartheta_i = \psi_i^l - \psi_i^s = \theta_i^l e^{-i(wt+\varphi_i^l)} - (-1)^i \theta_i^s e^{-i(wt+\varphi_i^s)}. \quad (4)$$

Based on the Lagrangian method (See **Supplementary Equations (1) – (28)** in **Supplementary Note1** for the derivation process), we can obtain the longitudinal displacement $u_i$ and rotational displacement $\vartheta$. In this way, one can see that the inertial matrix (**Supplementary Equation (17)**) and stiffness matrix (**Supplementary Equations (18) – (25)**) are similar but not identical to current reported results[13]. According to the above analysis, the theoretical transmission (as denoted by the red solid line in Figure 2(b)) and dispersion spectrum (Figure 2 (c)) can be obtained directly. However, the inertial amplification cannot be observed in the inertial matrix (**Supplementary Equation (17)**). The wave equation only reveals one fact, i.e., the longitudinal polarization is coupled with torsional polarization. However, it has been demonstrated that only specific couplings (such as the syndiotactic PnCs [8, 14]) rather than all couplings can give rise to such a bandgap [14, 16]. Therefore, the explanation of the coupling[13] needs to be clarified further.

It is worth noting that, $P_{lb} + P_{rb}$ and $P_{ls} + P_{rs}$ are two independent wave modes. Therefore, it allows us to regard $u_i^b$, $u_i^s$, $\psi_i^b$, and $\psi_i^s$ as the independent variables, similarly, based on the Lagrangian method (See **Supplementary Equations (29) – (39)** in **Supplementary Note1** for the derivation process), as a result, the inertial matrix and stiffness matrix will be significantly different, as illustrated by **Supplementary Equations (31) – (34)**. Based on **Supplementary Equations (31) – (39)** and physical parameters listed in **Supplementary Note5**, we can also obtain the theoretical transmission (as denoted by the blue dashed line in Figure 2(b)), which is consistent with the numerical results. Figure 2(b) illustrates that both paths of establishing wave equations can yield identical transmissions to the numerical results.

However, in contrast to the former classical theory (**Supplementary Equations (17) – (27)**), several essential information can be captured in the latter derivation method. First, as denoted by **Supplementary Equations (35) – (37)**, the stiffness matrix does not indicate the coupling effect between longitudinal polarization and rotational polarization, but the inertial matrix does. Second, the inertial matrix (**Supplementary Equations (31) – (34)**) will reveal the existence of inertial amplification, which is derived from the coupling effect. Third, both bending and stretch modes can realize the motion coupling and thus obtain the inertial amplification effect, as denoted by $p$ in **Supplementary Equation (32)** and $q$ in **Supplementary Equation (34)**. Fourth, the motion coupling guided by the bending mode is characterized by longitudinal polarization (because the primary diagonal element of $\mathrm{M}_{11}$ includes $m_i$ and the non-diagonal element is $I_i$), while the motion coupling guided by the stretch mode is characterized by the rotational mode (because the primary diagonal element of $\mathrm{M}_{22}$ includes $I_i$ and the secondary diagonal element is $m_i$).

At this point, we can learn about that the bandgap in the chiral PnCs must be accompanied by two wave modes that will truncate the bandgap range. These two wave modes are similar to the acoustic mode and optic mode of the classical diatomic chain, as shown in Figure 1(f), which together determine the bandgap range (Figure 1(i)). Therein, the two atoms of the diatomic unit cell vibrate in the same phase as an acoustic mode (as illustrated by Figure 1(g)), while the two atoms vibrate with opposite phases as an optic mode (as illustrated by Figure 1(h)). The same phenomena can be observed in the chiral PnC, as illustrated in Figures 1(c) and 1(d). According to the left-handed feature of the subunit cell, under the longitudinal input $P_i$, the first expected case is the longitudinal motion of the disk Ⅱ accompanied by a rotation around the $-z$-axis (Based on the right-hand spiral rule), as shown in Figure 1(c), which corresponds to the acoustic mode in the classical diatomic chain. Similarly, for the optic mode, as shown in Figure 1(d), the longitudinal motion of the $m_2$ is accompanied by a rotation around $+z$-axis, which corresponds to

the optic mode in the classical diatomic chain. Therefore, the lower boundary of the bandgap in chiral PnCs can be named the acoustic branch (the two red pass bands in Figure 2(c)) since the vibration in the phase of adjacent atoms, and the upper boundary can be named the optic branch (the two blue pass bands in Figure 2(c)) because it is similar to that in the long-wavelength limit of an optic mode [22]. The bandgap will convert into Bragg scattering type after the optic branch [23].

Besides, the numerical deformation contours also demonstrate the similarity between the theoretical wave modes and the classical diatomic chain, as shown in Figure 2(f). The rotational directions of $p_{u1}$ & $p_{u2}$ are opposite to that of $p_{l1}$ & $p_{l2}$ when the translation is along $+z$-axis, which exactly corresponds to the schematics in Figure 1(c) and Figure 1(d), respectively. For instance, comparing Figure 1(c) to the mode $P_{l1}$, one can see that Figure 1(c) shows a rotation around $-z$-axis and a translation along $-z$-axis since the bending along $-z$-axis, and $P_{l1}$ in Figure 2(f) shows a rotation around $+z$-axis and a translation along $+z$-axis due to bending along $-z$-axis. The schematics of the rotation and translation phases are completely identical to those of the simulation ones. Similarly, Figure 1(d) shows a rotation around $+z$-axis and a translation along $-z$-axis since the compression, and $P_{u1}$ in Figure 2(f) shows a rotation around $-z$-axis and a translation along $+z$-axis due to stretch. These two have excellent consistency.

It is crucial to emphasize that these acoustic and optic branches essentially differ from conventional diatomic chains. In detail, the upper and lower branches in this context stem from two coupled orthogonal motions that originate from the same atom instead of from two atoms. Coincidentally, this coupled orthogonal polarization introduces a novel control variable for bandgap modulation — inertial amplification [12], as compared by Figure 1(b) and Figure 1(e). Nevertheless, the inertial amplification effect will be hidden in the wave equation if we utilize the traditional theoretical derivation directly based on force equilibrium.

It should be noted that there is a discrepancy between the expected bandgap width of the dispersion spectrum and the attenuation range of the transmission. The expected bandgap covers 500 Hz – 1700 Hz, while the attenuation range shown in the transmission (Figure 2(b)) only appears in 500 Hz – 1400 Hz. This is due to the different boundary conditions in calculating the dispersion spectrum and the transmission. For the calculation of the dispersion spectrum, all the unit cell is free. For the calculation of the transmission, the rotation freedom of the first lumped mass is constrained. If we release this degree of freedom, the attenuation range will be 500 Hz – 1700 Hz, corresponding to the expected bandgap width (Please see **Supplementary Note6** for more details.). Overall, the consistency in transmissions (Figure 2(b)), dispersion spectra Figure 2(c), as well as the deformation schematics (Figure 1(c), Figure

1(c), &Figure 2(f)), can verify the correctness of our analysis.

Another essential advantage of our method is that, as illustrated by **Supplementary Equations (38)**, we can directly obtain the longitudinal amplitude $u_i^b$ determined by the bending deformation and the rotational amplitude $\psi_i^s$ determined by the stretch deformation. Furthermore, by substituting the results of **Supplementary Equation (38)** into **Supplementary Equation (14)**, we can obtain the rotational amplitude $\psi_i^b$ determined by the bending deformation and the longitudinal amplitude $u_i^s$ determined by the stretch deformation. In other words, we can observe the respective contributions and influences of the acoustic mode and the optic branch on the bandgap. As shown in Figures 2(d) and 2(e), the acoustic mode is dominant before the anti-resonance notch in the bandgap. After that, the optic mode will dominate the transmission coefficient. Although Figure 2(e) shows that $R_b$ has almost the same relative amplitude as $R_s$ after the anti-resonance notch, it can be regarded as passive for $R_b$ to present the large amplitude according to the causal inference in **Supplementary Note1**. More simply, if we can shift the optic mode towards a higher frequency, this passive effect originates from $R_s$ to $R_b$ will be much weaker, and the frequency range dominated by $u_b$ will be broader, which can be demonstrated in the section about Figure 4.

In short, for chiral PnCs [24, 25], it is convenient and concise to characterize the dispersion spectrum and transmission properties through the wave equation established from force equilibrium, but its final formulas merely present the coupled longitudinal and rotational polarizations, thus obscuring the comprehensive physical insights. Consequently, despite the observations of the similar coupling orthogonal polarizations in two-dimensional and three-dimensional chiral structures [26, 27, 28] which are characterized by auxeticity in quasi-static compression [29], and even the systematical establishment of the governing equations [30, 31, 32], there have been limited discoveries of inertial amplification. In the end, many studies stagnated at the bandgap opening due to the limitations of the structural shape evolution [8, 11, 33, 34].

## b) Coupling roots of acoustic and optic branches

As observed in the wave equation we proposed, the inertial amplification is a unique and essential advantage for the chiral PnCs. However, broadening the bandgap is extremely challenging since there must be the optic branch. To clarify the challenge, we neglect the contribution of stretch mode ($P_{ls}$ and $P_{rs}$) and consider the bending mode only based on the method shown in **Supplementary Equations (29) – (39)**. The theoretical transmission (the blue line in Figure 2(a)) is still consistent with the numerical results in low frequencies, and the dynamic equation can also reveal the inertial amplification effect, as demonstrated by other report[15]. This indicates that bending mode ($P_{lb}$ and

$P_{rb}$) directly determines the existence of the bandgap, and the stretch mode ($P_{ls}$ and $P_{rs}$) determines the upper limit of the bandgap.

The comparison of Figures 2(a) and 2(b) might lead us to believe that the main contribution of stretch mode is only to truncate the inertial amplification-based bandgap, but that is is not completely true. This bandgap formation relies on the coupled longitudinal-rotational motions of each lumped mass. In the conventional unit cell, although the longitudinal motion and rotational motion originate from the bending deformation of the ligaments, **Supplementary Note3** illustrated that, for the solid structure, the bending mode will be absent if the stretch mode does not exist because both modes are determined by the identical basic physical and geometric parameters. Therefore, it seems impossible to make the optic modes disappear completely to obtain an infinite bandgap. Therefore, it is vital to figure out the coupling between optic and acoustic modes as well as find ways to manipulate them independently.

Figure 2(a) illustrates that the bending mode serves to provide the stiffness $k_b$ and inertial amplification coefficient $p$. $k_b$ and $p$ are critical for directly determining the acoustic branch. The comparison of Figure 2(a) and Figure 2(b) illustrates that the stretch mode determines the optic branch by the stiffness $k_s$ and $q$. Therefore, for a normalized low-frequency and broad bandgap, $p$ and $k_s$ should be larger while $q$ should be larger, and $k_b$ should be constant to provide sufficient support capacity.

However, contrary to expectations, the actual situation is unfavorable. In details, on the one hand, Figure 1(c) and Figure 1(d) illustrated that, $P_{rb}$ and $P_{rs}$ have the opposite directions, which implies a hybridization between the rotational polarizations determined by bending and stretch modes. If there is no hybridization between $p$ and $q$, (see **Supplementary Note3** and **Supplementary Note4** for more details)

$$p = \tan\gamma\,. \tag{5}$$

The ideal inertial amplification coefficient will vary like the blue line shown in Figure 3(a). One can see that the amplified dynamic inertia $p$ would easily exceed 100 times.

If considering the hybridization, $p$ is written as (see **Supplementary Note3** and **Supplementary Note4** for more details)

$$p = \frac{\Delta R_b - \Delta R_s}{\Delta u_b + \Delta u_s} \tag{6}$$

where $\Delta u_b$ refers to the longitudinal displacement difference (between $m_i$ and $m_{i-1}$) caused by the bending mode under the longitudinal harmonic loads; $\Delta u_s$ refers to the longitudinal displacement difference caused by the stretch mode under the longitudinal harmonic loads; $\Delta R_b$ refers to the rotational displacement difference caused by the

bending mode under the longitudinal harmonic loads; $\Delta R_s$ refers to the rotational displacement difference caused by the stretch mode under the longitudinal harmonic loads.

From Eq. (6), if $\Delta R_s$ is larger with the increase of $\Delta u_s$, $p$ will be smaller, which will reduce the inertial amplification effect. This is a hybridization between $q$ and $p$ ((see **Supplementary Equations (40), (41), (42)**, and **(45)** for more details)). Considering the hybridization, the amplified dynamic inertia $p$ can only be at most 2.6 times.

On the other hand, as illustrated by Figure 3(b), $k_b$ will increase rapidly with the increase of $\theta$. Then, the difference between $k_b$ and $k_s$ will be smaller and smaller, which is not conducive to achieving a broad bandgap [13]. Ultimately, the upper boundary will approach the lower boundary of the bandgap, leading to the closure of the bandgap, as depicted in Figure 3(c). For instance, if we need the maximum inertial amplification (when $\theta$ is about 80°) to reduce the bandgap, then the stiffness difference between $k_s$ and $k_b$ is only 1.76 times. These two aspects denote a significant contradiction between the broad bandgap and the low-frequency bandgap.

## c) Customization of acoustic and optic branches

To resolve the contradiction, we propose the strategy, as shown in Figure 4(a), to achieve partial decoupling. As illustrated in Figure 4(b), the subunit cell can be divided into three components, i.e., the lumped disks, the spiral springs, and spherical hinges. Figure 4(c) shows a detailed schematic of the spherical hinges, and its governing equation can be found in **Supplementary Note7**. In this unit cell, the spiral springs provide $k_b$ and the spherical hinges are responsible for providing the rotational polarization while the spiral springs are compressed, thus achieving $p$. Therefore, $k_s$ is determined by the spherical hinges. Regarding the unit cell, its first bandgap extending from 39 Hz – 1650 Hz can be obtained in the dispersion spectrum (in Figure 4(d)) (see **Supplementary Method1** for more details of the simulation). The ratio of the lower boundary of the optic branch to the upper boundary of the acoustic branch is up to 42 times.

To validate our proposed design under controlled conditions and minimize the influence of extraneous factors, thus ensuring experimental validity, one unit cell was fabricated and subjected to rigorous testing as illustrated in Figure 4(a). To avoid the local resonance modes of the lumped masses, the end of the period direction is replaced by a carbon fiber plate, which can provide a high elastic modulus with a low density (See Method for more details of the experiment). The experimental and numerical results are shown in Figure 4(d). One can see that there is an obvious attenuation after 35 Hz, and the experimental and numerical results are in satisfying agreement in 100 Hz, especially at resonance peaks ($P_1$ and $P_2$) and anti-resonance notches ($N_1$ and $N_2$). There are significant deviations between

numerical and experimental results after 100 Hz, which might be resulted by the nonlinear collisions from the clearance in the spherical hinge [35].

Regarding the PnC shown in Figure 4(a), the material of the spherical hinge is steel, while that of the springs is Nylon, and the springs are spiral to further decrease the equivalent stiffness $k_s$, affording $k_s$ and $k_b$ great discrepancy. On the one hand, the discrepancy is beneficial in raising the optic branch and thus broadening the bandgap. On the other hand, because of the great discrepancy between $k_s$ and $k_b$, the deformation ($\Delta R_s$ and $\Delta u_s$) of the stretch mode will be much weaker, so the hybridization to $p$ will be weakened. Therefore, the numerical inertial amplification coefficient $p$ can be up to 13 times with the increase of the tilt angle $\theta$, as shown in Figure 5(a) (the original coefficient is a maximum of 2.6). In this case, the lower boundary will shift to a lower frequency while the upper boundary can be almost constant, as Figure 5(b) shows.

In addition, because the functions of the spiral springs and spherical hinges are independent, the disparity between $k_s$ and $k_b$ can be magnified by variations in the material and dimensions of the spherical hinges. Consequently, with the increase in the stiffness ratio ($k_s/k_b$ where $k_b$ is constant), the bandgap width can be expanded (Figure 5(c)), where the upper boundary will shift to a higher frequency while the lower boundary is constant.

In brief, compared to conventional unit cells, this unit cell with the spherical hinges enables the attainment of low-frequency and wide bandgaps by tuning the inclination angle $\theta$ and the material and geometric properties of the spherical hinges, while significantly mitigating the constraints imposed by the equivalent supporting stiffness $k_b$, equivalent density, and lattice constant. While this work showcases realization in broad and low-frequency bandgaps, it should be acknowledged that enhancing the attenuation intensity of the inertial amplification-based bandgap will be the next significant challenge [15].

## Conclusions

In summary, in this research, we have theoretically revealed that the inertial amplification effect evolves from inertia matrix to stiffness matrix, thus unifying two ostensibly conflicting explanations of the bandgap mechanism. Based on our theory, which allows to observe the comprehensive physics of acoustic and optic branches in chiral PnCs, we have clarified that the close relations between the rise of the inertial amplification coefficient and the bending and stretch stiffness, as well as the restrictions from this close relations on the creation of broad subwavelength bandgaps under boundaries constrained by the constant equivalent density, equivalent stiffness, and lattice constant. Therefore, we have used spherical hinges to achieve the partial decouple, thus releasing the mutual

negative effect between the acoustic and optic boundaries. The numerical and experimental results have confirmed the effectiveness of our proposed scheme and demonstrated that the underlying physics obtained from the wave behavior is instructive for structural design. This work may be able to shield light on the discovery of the inertial amplification effects in other high-dimensional artificial structures, to realize ultra-low-frequency and ultra-broad bandgaps without the requirement of the bulky static mass and fragile static stiffness, as well as to customize the bandgap in chiral PnCs.

## Method

### Experiment Configuration and Boundary Conditions

The input disk is bolted to a plexiglass with a thickness of 15 mm, and the plexiglass must have approximately ten times the weight of the bottom disk to limit the freedom of rotation of the disk around the z-axis as much as possible. The shaker is excited directly on the plexiglass through the excitation bar to stimulate the harmonic excitation. Two acceleration sensors (PCB 353B15) are attached to the top and the bottom of the sample to pick up the output acceleration $a_o$ and the input acceleration $a_i$, respectively. The experimental transmission is calculated by $a_o/a_i$. The frequency range of the sine sweep is divided into three bands, i.e., 10 Hz – 200 Hz, 200 Hz - 1000 Hz, and 1000 Hz – 3000 Hz, to avoid exceeding the allowable amplitude of the shaker under different voltages and to guarantee the output acceleration $a_o$ is higher than the background noise. The frequency resolution is 2 Hz, and the sweeping speed is 200 Hz/min, to guarantee the precision of experimental data.

## Data availability

The data that support the findings of this study are available from the corresponding author upon reasonable request.

## Code availability

The code used to generate the data used in this study is available from the corresponding author upon reasonable request

## Acknowledgements

This work was financially supported by the National Natural Science Foundation of China (No. 12002258), the State Key Laboratory for Strength and Vibration of Mechanical Structures (No. SV2023-KF-08), and the China Postdoctoral Science Foundation (No. 2022M712540). Wei Ding is grateful for the support of the China Scholarship

Council (No. 202206280170). Wei Ding appreciates Yuhan Hu (Hohai University) for her guidance in drawing.

## Author contributions

W. D. and R. Z. proposed the concept and performed the theoretical analysis, numerical calculation, and experimental demonstration. T.N.C. and J.Z. provided the experimental sponsorship. W.D., R.Z, and J. Z. wrote the manuscript and the Supplementary Information. J.Z, Y.W.Y, and B.A guided the research. S.Q., D.W.Y., and L.W.D. processed the data and organized the manuscript. All the authors contributed to the discussion of the results.

## Competing interests

The authors declare no competing interests.

## References

1.Bossart A, Fleury R. Extreme Spatial Dispersion in Nonlocally Resonant Elastic Metamaterials. Phys. Rev. Lett. **130**, 207201 (2023).

2.Babaee S, Overvelde JT, Chen ER, Tournat V, Bertoldi K. Reconfigurable origami-inspired acoustic waveguides. Science Advances **2**, e1601019 (2016).

3.Fu Y*, et al.* Asymmetric Generation of Acoustic Vortex Using Dual-Layer Metasurfaces. Phys. Rev. Lett. **128**, 104501 (2022).

4.Maldovan M. Narrow Low-Frequency Spectrum and Heat Management by Thermocrystals. Phys. Rev. Lett. **110**, 025902 (2013).

5.Van Damme B, Hannema G, Sales Souza L, Weisse B, Tallarico D, Bergamini A. Inherent non-linear damping in resonators with inertia amplification. Appl. Phys. Lett. **119**, 061901 (2021).

6.Yilmaz C, Hulbert GM. Theory of phononic gaps induced by inertial amplification in finite structures. Phys. Lett. A **374**, 3576-3584 (2010).

7.Otlu SN, Acar B, Tetik ZG, Yilmaz C. Three-dimensional ultra-wide elastic metamaterial with inertial amplification mechanisms having optimized flexure hinges. Int. J. Solids Struct. **282**, 112453 (2023).

8.Zhao P, Zhang K, Hong F, Deng Z. Tacticity-based one-dimensional chiral equilateral lattice for tailored wave propagation and design of elastic wave logic gate. J. Sound Vib. **521**, 116671 (2022).

9.Zhou Y, Ye L, Chen Y. Investigation of novel 3D-printed diatomic and local resonant metamaterials with impact mitigation capacity. Int.l J. Mech. Sci. **206**, 106632 (2021).

10.Yilmaz C, Hulbert GM, Kikuchi N. Phononic band gaps induced by inertial amplification in periodic media. Phys. Rev. B **76**, 054309 (2007).

11.Zhao P, Zhang K, Qi L, Deng Z. 3D chiral mechanical metamaterial for tailored band gap and manipulation of vibration isolation. Mech. Syst. Sig. Process. **180**, 109430 (2022).

12.Ding W*, et al.* Description of Bandgaps Opening in Chiral Phononic Crystals by Analogy with Thomson scattering. New J. Phys. **25**, 103001 (2023).

13.Park J, Lee D, Jang Y, Lee A, Rho J. Chiral trabeated metabeam for low-frequency multimode wave mitigation via

dual-bandgap mechanism. Commun. Phys. **5**, 194 (2022).

14.Bergamini A*, et al.* Tacticity in chiral phononic crystals. Nat. Commun. **10**, 4525 (2019).

15.Orta AH, Yilmaz C. Inertial amplification induced phononic band gaps generated by a compliant axial to rotary motion conversion mechanism. J. Sound Vib. **439**, 329-343 (2019).

16.Zheng B, Xu J. Mechanical logic switches based on DNA-inspired acoustic metamaterials with ultrabroad low-frequency band gaps. J. Phys. D: Appl. Phys. **50**, 465601 (2017).

17.Oh JH, Qi S, Kim YY, Assouar B. Elastic Metamaterial Insulator for Broadband Low-Frequency Flexural Vibration Shielding. Phys. Rev. Appl. **8**, 054034 (2017).

18.Zhao C, Zhang K, Zhao P, Hong F, Deng Z. Bandgap merging and backward wave propagation in inertial amplification metamaterials. Int.l J. Mech. Sci. **250**, 108319 (2023).

19.Phani AS, Woodhouse J, Fleck NA. Wave propagation in two-dimensional periodic lattices. J. Acous. Soc. Am. **119**, 1995-2005 (2006).

20.Bravo T, Maury C. Causally-guided acoustic optimization of single-layer rigidly-backed micro-perforated partitions: Theory. J. Sound Vib. **520**, 116634 (2022).

21.Yang M, Chen S, Fu C, Sheng P. Optimal sound-absorbing structures. Materials Horizons **4**, 673-680 (2017).

22.Patterson JD, Bailey BC. *Solid-state physics: introduction to the theory*. Springer Science & Business Media (2007).

23.Yilmaz C, Kikuchi N. Analysis and design of passive low-pass filter-type vibration isolators considering stiffness and mass limitations. J. Sound Vib. **293**, 171-195 (2006).

24.Ding W*, et al.* Isotacticity in chiral phononic crystals for low-frequency bandgap. Int.l J. Mech. Sci. **261**, 108678 (2023).

25.Ding W, Chen T, Chen C, Chronopoulos D, Zhu J, Assouar B. Thomson scattering-induced bandgap in planar chiral phononic crystals. Mech. Syst. Sig. Process. **186**, 109922 (2023).

26.Foehr A, Bilal OR, Huber SD, Daraio C. Spiral-Based Phononic Plates: From Wave Beaming to Topological Insulators. Phys. Rev. Lett. **120**, 205501 (2018).

27.Lakes R. Deformation mechanisms in negative Poisson's ratio materials: structural aspects. Journal of Materials Science **26**, 2287-2292 (1991).

28.Dudek KK, Gatt R, Wojciechowski KW, Grima JN. Self-induced global rotation of chiral and other mechanical metamaterials. Int. J. Solids Struct. **191-192**, 212-219 (2020).

29.Mizzi L, Spaggiari A. Novel chiral honeycombs based on octahedral and dodecahedral Euclidean polygonal tessellations. Int. J. Solids Struct. **238**, 111428 (2022).

30.Liu XN, Huang GL, Hu GK. Chiral effect in plane isotropic micropolar elasticity and its application to chiral lattices. J. Mech. Phys. Solids **60**, 1907-1921 (2012).

31.Spadoni A, Ruzzene M. Elasto-static micropolar behavior of a chiral auxetic lattice. J. Mech. Phys. Solids **60**, 156-171 (2012).

32.Bacigalupo A, Gambarotta L. Simplified modelling of chiral lattice materials with local resonators. Int. J. Solids Struct. **83**, 126-141 (2016).

33.Yin C, Xiao Y, Zhu D, Wang J, Qin Q-H. Design of low-frequency 1D phononic crystals harnessing compression–twist coupling effect with large deflection angle. Thin. Wall. Struct. **179**, 109600 (2022).

34.Baravelli E, Ruzzene M. Internally resonating lattices for bandgap generation and low-frequency vibration control. J. Sound Vib. **332**, 6562-6579 (2013).

35.Fang X, Wen J, Bonello B, Yin J, Yu D. Ultra-low and ultra-broad-band nonlinear acoustic metamaterials. Nat. Commun. **8**, 1288 (2017).

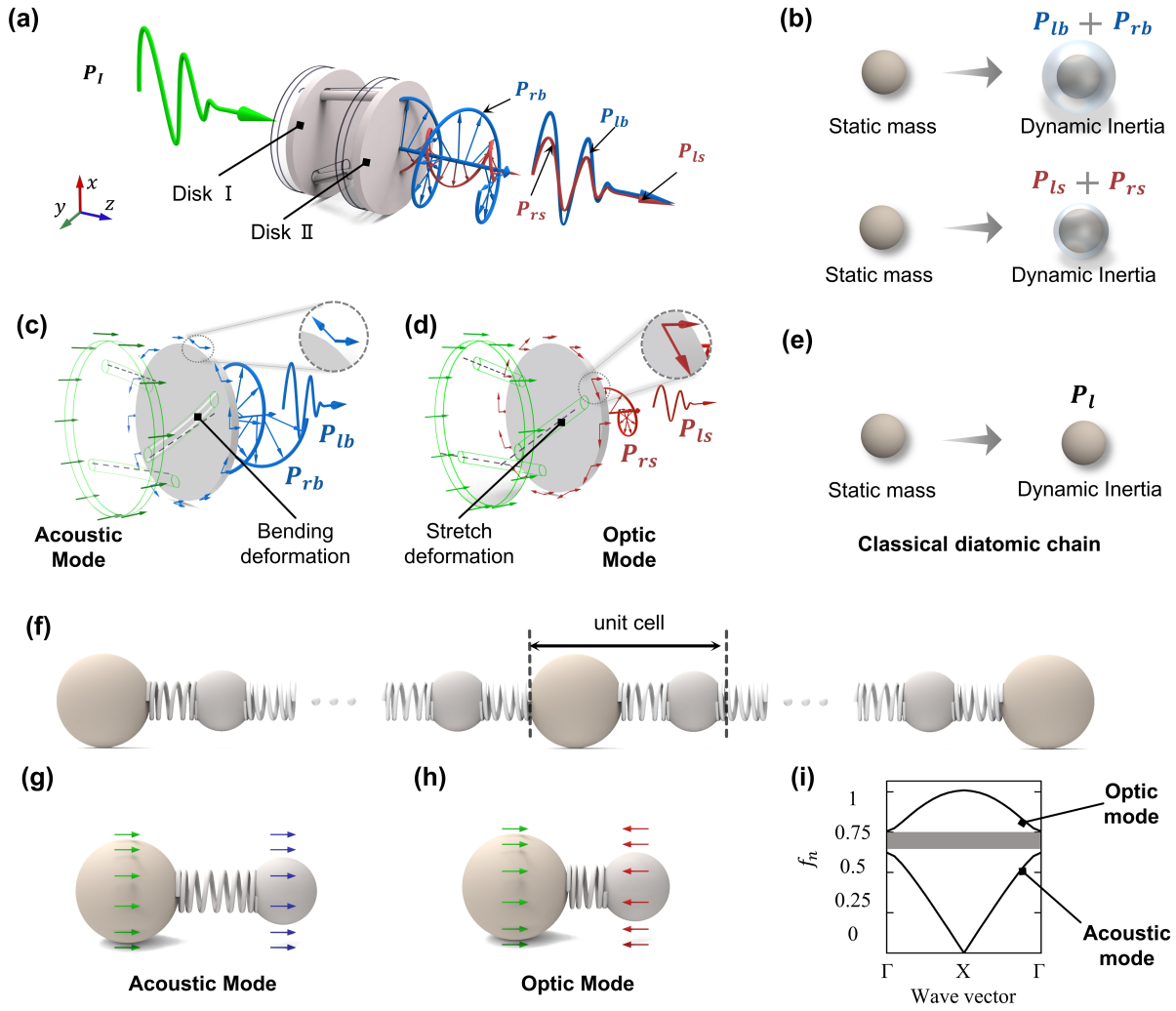


**Figure 1. Acoustic and optic modes in the chiral PnC and its comparison with classical diatomic chains.** (a) Schematics of the conventional chiral subunit cell and its macroscopic polarizations under the longitudinal input $\boldsymbol{P_I}$. The green arrow denotes the longitudinal input mode; the blue arrows denote the polarizations determined by the bending deformation of the ligaments; the red arrows denote the polarizations determined by the stretch deformation of the ligaments. (b) The difference between the static mass and the dynamical inertia in the chiral subunit cell. The gray shadow refers to the extra inertia induced by the polarization coupling, such as $\boldsymbol{P_{lb}} + \boldsymbol{P_{rb}}$ as well as $\boldsymbol{P_{ls}} + \boldsymbol{P_{rs}}$. (c) Polarizations of the acoustic mode determined by the bending deformation of the ligaments. (d) Polarizations of the optic mode determined by the stretch deformation. (e) The relation between the static mass and the dynamical inertia in the classical diatomic chain. $\boldsymbol{P_l}$ means there is only longitudinal polarization in the classical diatomic chain. (f) Schematic of the classical diatomic chain. (g) – (h) Acoustic and optic modes in the classical diatomic unit cell. (i) Dispersion-spectrum schematic of the classical diatomic unit cell. Therein, the shading area indicates the bandgap.

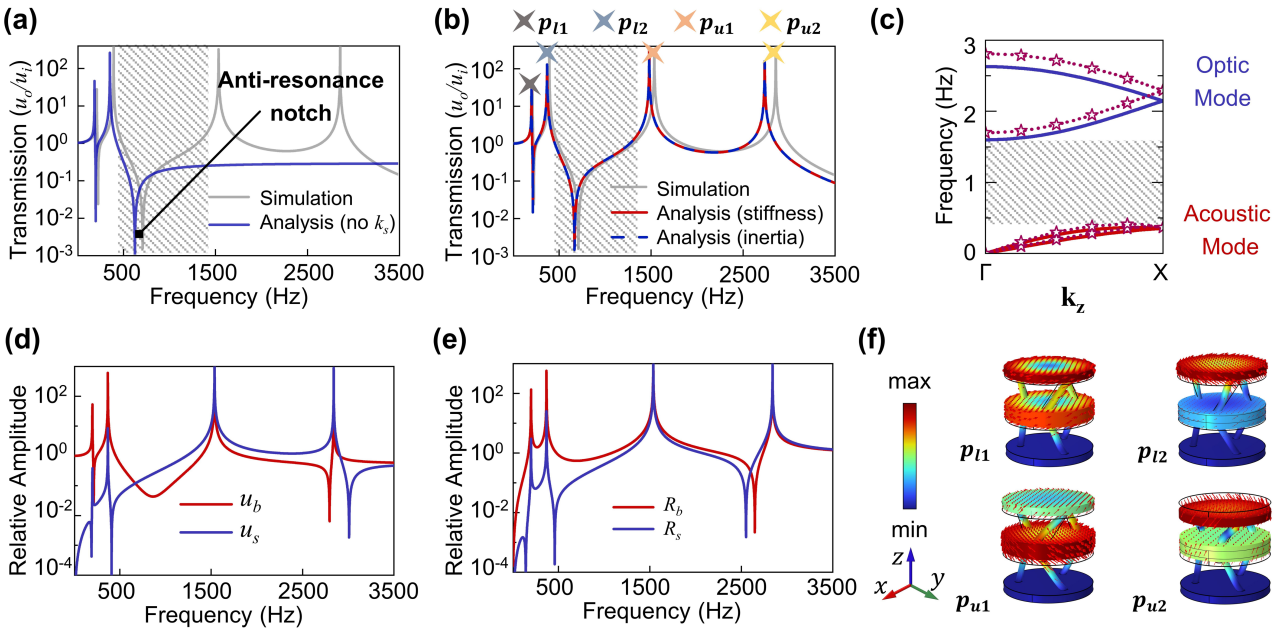


**Figure 2. Dynamics of the conventional chiral PnC.** (a) – (b) Theoretical and numerical transmissions of the conventional chiral PnCs. The gray line is the numerical results, and the others are the theoretical results. Therein, "no $\boldsymbol{k_s}$" denotes the results of neglecting the stretch mode; the red and blue lines in (b) are the results of considering the stretch mode, where the word "stiffness" in braces denotes that the result is obtained based on **Supplementary Equations (17) – (28)**, and the word "inertial" denotes that the theoretical result is obtained based on **Supplementary Equations (29) – (39)**. (c) Theoretical and numerical dispersion spectra (see **Supplementary Note2** for the governing equation of dispersion spectrum). Therein, the gray star-shaped dotted lines are the numerical dispersion curves and the others refers to the theoretical dispersion curves. The gray shading refers to the bandgap range. (d) The relative amplitudes of the longitudinal displacement. Therein, $\boldsymbol{u_b}$ and $\boldsymbol{u_s}$ refer to the relative longitudinal displacement induced by the bending and stretch modes, respectively. The relative amplitude is calculated by dividing the absolute amplitude by the input amplitude. The subscript "b" refers to the bending mode and "s" refers to be the stretch mode. (e) The relative amplitudes of the rotational displacement. Therein, $\boldsymbol{R_b}$ and $\boldsymbol{R_s}$ refer to the relative rotational displacement induced by the bending and stretch modes, respectively. The relative amplitude is calculated by dividing the absolute amplitude by the input amplitude. (f) Displacement contours for the upper and lower boundaries of the bandgap.

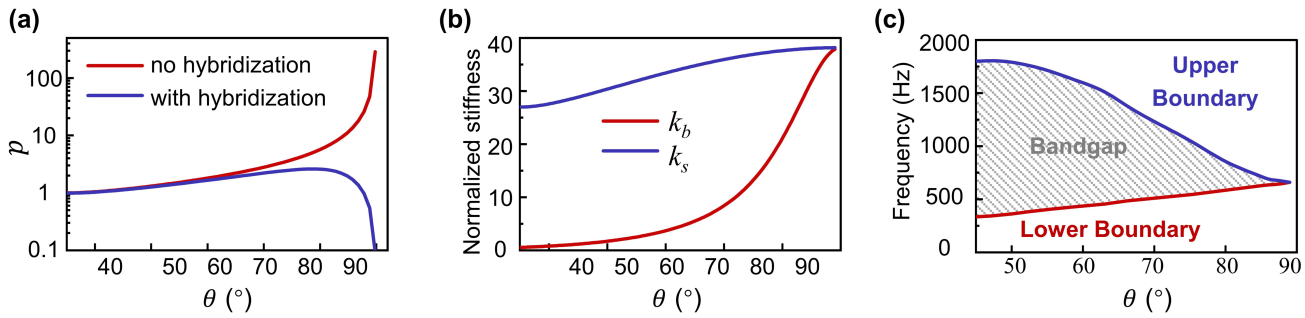


**Figure 3. Dependence of fundamental physical parameters of acoustic and optic branches on the angle $\boldsymbol{\theta}$.** (a) – (c) Parameter discussion about the influence of $\boldsymbol{\theta}$ on the inertial amplification coefficient $\boldsymbol{p}$, bending stiffness $\boldsymbol{k_b}$, and stretch stiffness $\boldsymbol{k_s}$ of conventional chiral PnCs. The abbreviation "Nor." means the word "normalization", i.e., $\boldsymbol{k/k_r}$ where $\boldsymbol{k_r = 1e5\ \ N\,m^{-1}}$ (See **Supplementary Note3** for more details of $\boldsymbol{\theta}$ and for the governing equation about $\boldsymbol{k_b}$ and $\boldsymbol{k_s}$). (c) Bandgap variation with the different $\boldsymbol{\theta}$. Therein, the gray shading is the bandgap ranges.

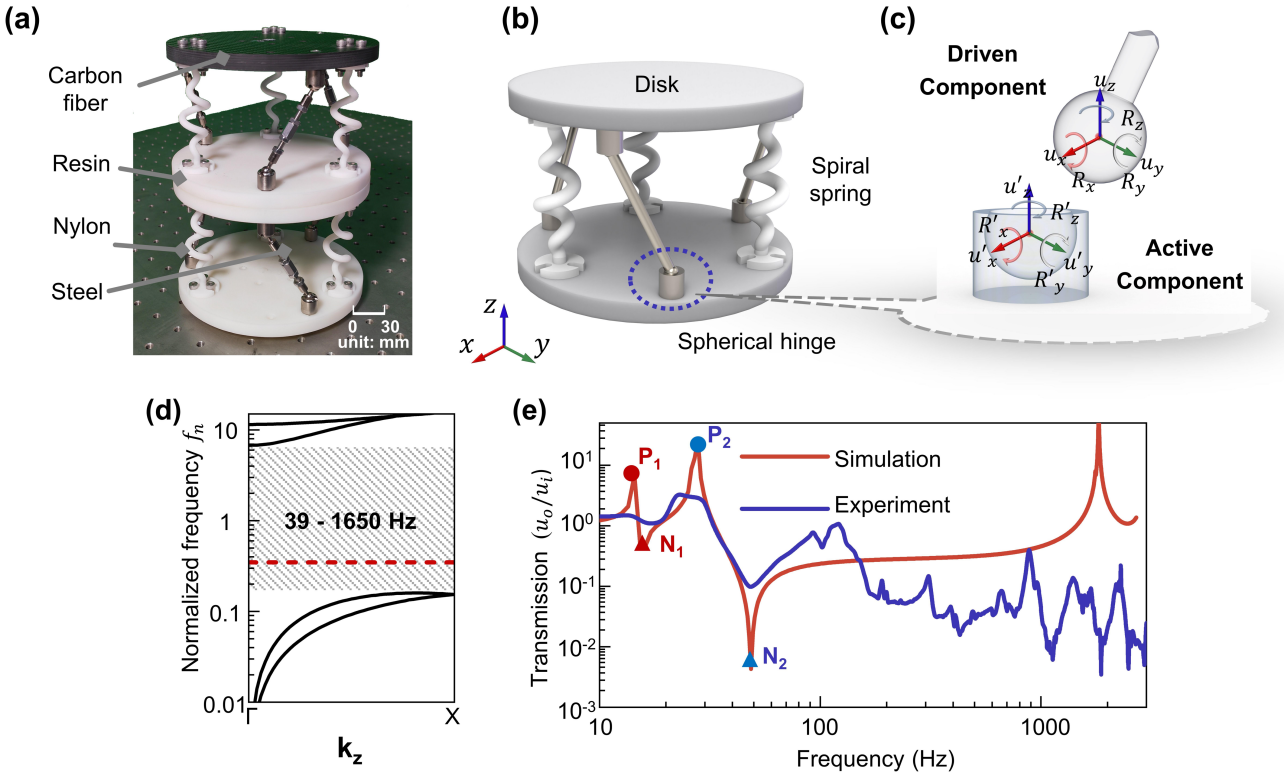


**Figure 4. Optimized chiral PnCs and its dynamic properties.** (a) Photograph of the experimental sample (See Method for experimental details). (b) Schematics of the subunit cell (See **Supplementary Figure1** for details about geometry). (c) Schematic of the geometric relationship of the spherical hinges. See Supplementary S7 for the governing equations between the driven component and

active component of the spherical hinges. (d) Normalized dispersion spectra of the chiral PnCs. The red line is the starting frequency of the unit cell without spherical hinges, and it is 0.347 (88 Hz). The shading area indicates the bandgap range. Normalization method is $\boldsymbol{f_n = f/\left(\sqrt{k_b/m_e}\right)}$, where $\boldsymbol{m_e = 0.6018}$ kg and $\boldsymbol{k_b = 3.6e4}$ $\mathbf{N\ m^{-1}}$ (See **Supplementary Method2** for the reasons of the normalization method). (e) Numerical and experimental transmission of one unit cell. $\mathbf{P_1}$ and $\mathbf{P_2}$ denote the resonance peaks while $\mathbf{N_1}$ and $\mathbf{N_2}$ denote the anti-resonance notches.

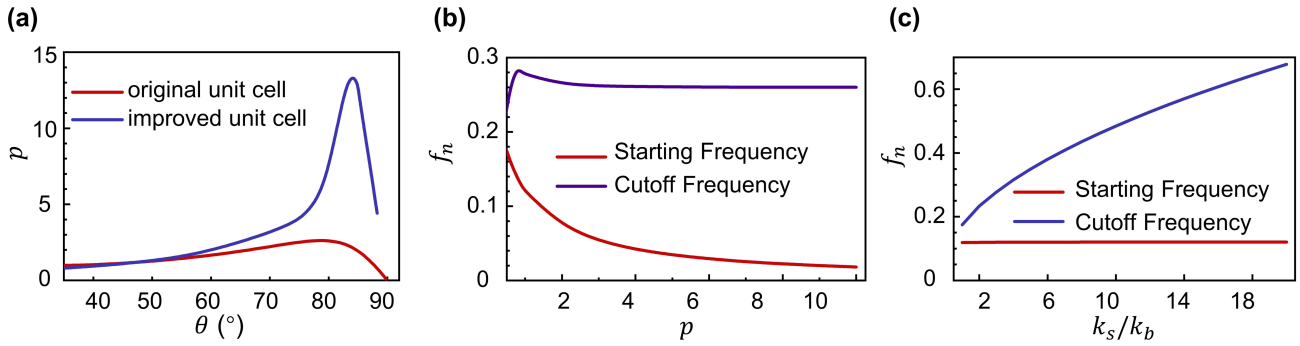


**Figure 5. Bandgap tuning of the improved unit cell.** (a) Variation of $p$ with different $\theta$. (b) – (c) Normalized bandgap width in different inertial amplification coefficients $p$ and different stiffness ratios ($k_s/k_b$). (See **Supplementary Method1** for details about the simulation).

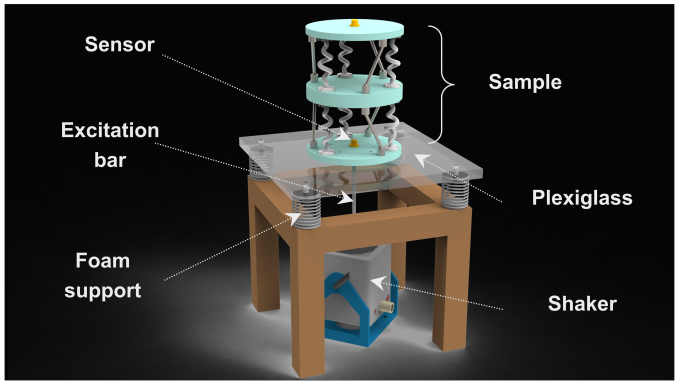


**Figure 6. Schematics of the experimental configuration for transmission test.** The bottom disk of the unit cell is bolted to a plexiglass. The two yellow domains indicate the acceleration sensors. The shaker is Modelshop-K2007E01, which is bolted to the optical platform and connected to the plexiglass thought an excitation bar. The foam support is used to isolate the vibration propagating from the optic platform to the plexiglass.